Ni-Rich Layered Cathode Materials with Electrochemo-Mechanically Compliant Microstructures for All-Solid-State Li Batteries

Sung Hoo Jung, Un-Hyuck Kim, Jae-Hyung Kim, Seunggoo Jun, Chong S. Yoon, Yoon Seok Jung,* and Yang-Kook Sun*

While Ni-rich cathode materials combined with highly conductive and mechanically sinterable sulfide solid electrolytes are imperative for practical all-solid-state Li batteries (ASLBs), they suffer from poor performance. Moreover, the prevailing wisdom regarding the use of Li[Ni,Co,Mn]O$_2$ in conventional liquid electrolyte cells, that is, increased capacity upon increased Ni content, at the expense of degraded cycling stability, has not been applied in ASLBs. In this work, the effect of overlooked but dominant electrochemo-mechanical on the performance of Ni-rich cathodes in ASLBs are elucidated by complementary analysis. While conventional Li[Ni$_{0.80}$Co$_{0.16}$Al$_{0.04}$]O$_2$ (NCA80) with randomly oriented grains is prone to severe particle disintegration even at the initial cycle, the radially oriented rod-shaped grains in full-concentration gradient Li[Ni$_{0.75}$Co$_{0.10}$Mn$_{0.15}$]O$_2$ (FCG75) accommodate volume changes, maintaining mechanical integrity. This accounts for their different performance in terms of reversible capacity (156 vs 196 mA h g^{-1}), initial Coulombic efficiency (71.2 vs 84.9%), and capacity retention (46.9 vs 79.1% after 200 cycles) at 30 °C. The superior interfacial stability for FCG75/Li$_6$PS$_5$Cl to for NCA80/Li$_6$PS$_5$Cl is also probed. Finally, the reversible operation of FCG75/Li ASLBs is demonstrated. The excellent performance of FCG75 ranks at the highest level in the ASLB field.

1. Introduction

Currently, progress in the use of conventional lithium-ion batteries (LIBs) for the electrification of powertrains faces serious challenges. The use of flammable organic liquid electrolytes (LEs) for LIBs raises serious safety concerns.[1–5] Moreover, the exploitation of alternative electrode chemistries, such as Li metal for LIBs, has been hindered by the intrinsically limited properties of LEs.[1,6,7] For these reasons, the solidification of electrolytes with non-flammable and single-ion conducting inorganic solid electrolytes (SEs) is highly desired.[2,8–15] Among various SE material candidates, the highest ionic conductivities comparable to those of LEs (≈10 mS cm^{-1} at room temperature) have been achieved for sulfide SEs (e.g., Li$_{10}$GeP$_2$S$_{12}$:[16] 12 mS cm^{-1}, Li$_7$P$_3$S$_{11}$:[17] 17 mS cm^{-1}, Li$_{5.5}$PS$_{4.5}$Cl$_{1.5}$:[18,19] 12 mS cm^{-1}). Importantly, sulfide SE materials are superior to their competitors, such as oxide SEs, in device integration as they can be deformed to wet active materials by simple cold-pressing, enabling scalable fabrication of composite electrodes for bulk-type all-solid-state batteries.[3,20,21]

The applicability of layered LiMO$_2$ (M=Co, Ni, Mn) cathode materials for SEs is at the heart of practical all-solid-state lithium battery (ASLB) technologies.[3,22–26] To date, extensive studies have been devoted to revealing the underlying interfacial electrochemistry for LiMO$_2$/SE.[27–33] Basically, due to the poor intrinsic electrochemical stability of sulfide SEs (<3 V vs Li/Li$^+$), their oxidative decomposition at the operating voltages for LiMO$_2$ is inevitable.[34,35] Moreover, the electrochemically driven formation of electronic conductors, such as Co$_3$S$_4$, as a component of undesirable mixed conducting interphases also contributes to the large interfacial resistances of LiCoO$_2$/sulfide SEs.[24,36] Protective surface coatings on LiCoO$_2$ with electronically insulating and Li$^+$-conducting materials, such as LiNbO$_3$ and Li$_{3-x}$B$_{1-x}$C$_x$O$_3$, have been developed to mitigate undesirable side reactions while minimizing the offset of retarded Li$^+$ movements across the interfaces,[16,24,32,37–39] which is also a common practice for conventional LIBs.[40]

Many previous studies on LiMO$_2$ for ASLBs focused on LiCoO$_2$.[2,3,16,20,24,26–28,30,32,35,37–39] The employment of state-of-the-art Ni-rich cathode materials for ASLBs aligns

Dr. S. H. Jung, U.-H. Kim, J.-H. Kim, S. Jun, Prof. Y. S. Jung,
Prof. Y.-K. Sun
Department of Energy Engineering
Hanyang University
Seoul 04763, Republic of Korea
E-mail: yoonsjung@hanyang.ac.kr; yksun@hanyang.ac.kr
Prof. C. S. Yoon
Department of Materials Science and Engineering
Hanyang University
Seoul 04763, Republic of Korea

The ORCID identification number(s) for the author(s) of this article can be found under https://doi.org/10.1002/aenm.201903360.

**ADVANCED
SCIENCE NEWS**

www.advancedsciencenews.com

**ADVANCED
ENERGY
MATERIALS**

www.advenergymat.de

with the research direction of achieving higher energy density and lower cost for advanced LE-based LIBs.[41–44] However, the transition from $LiCoO_2$ to $Li[Ni,Co,Mn]O_2$ (NCM) for ASLBs results in much poorer electrochemical performances than expected. Specifically, low utilization (low capacity ratio of the one with SEs to the one with LEs) and low initial Coulombic efficiencies (CEs) were obtained (Table S1, Supporting Information).[3,20,22,24,31,45–48]

For advanced LIBs, pushing the Ni content in NCM to the theoretical limit ($LiNiO_2$) to maximize the capacity is a main research and development stream in both academic and industrial viewpoints,[41–44,49] as found in the current battery chemistry in the Tesla Model S.[50] However, it has been challenged by the non-stoichiometric nature of $LiNiO_2$, the more severe side reactions with LEs associated with highly reactive Ni^{4+}, degraded thermal stability, and volumetric strain during charge–discharge.[42,43] Thus, the wisdom, that is, the increased capacity at the expense of degraded cycling and thermal stabilities upon increasing Ni content in NCM, might hold for ASLBs as well. Furthermore, in a previous work by Janek and co-workers, the importance of chemo-mechanics for all-solid-state batteries was suggested.[48] Only a few percent of volumetric strain in $LiMO_2$ during charge–discharge could lead to detachment from SEs.[46] This could explain the significant degradation in the electrochemical performance of NCM in ASLBs, including low initial CEs and fast capacity fading, which should be more severe for the case of using Ni-enriched NCM because of the correspondingly larger volumetric strain.[46] These aforementioned considerations indicate that the higher the Ni content in NCM is, the poorer the electrochemical performances of the ASLBs would be. Surprisingly, our preliminary screening tests of all-solid-state NCM/Li-In half-cells with different Ni contents have failed to demonstrate any distinct trends, that is, the clear correlation between capacity or cycling stability and Ni content (Figure S1 and Table S2, Supporting Information), indicating the lack of current understanding. Meanwhile, recent investigations on the microstructural evolution and design strategies of Ni-rich cathodes for advanced LIBs, which have distinctly different features from those of $LiCoO_2$,[43,51–53] have caught our attention as a possibly overlooked clue to solving the aforementioned puzzle in the ASLB field.

Herein, we show that, by comparing two different Ni-rich cathode materials—a commercial-grade $Li[Ni_{0.80}Co_{0.16}Al_{0.04}]O_2$ (NCA80) having randomly oriented grains and a full-concentration gradient $Li[Ni_{0.75}Co_{0.10}Mn_{0.15}]O_2$ (FCG75) having radially oriented rod-shaped grains—the overlooked electrochemo-mechanics of microstructures in Ni-rich cathode materials have a determining role in the electrochemical performances of ASLBs. Complementary analysis using electrochemical, ex situ and in situ X-ray diffraction (XRD), operando electrochemical pressiometry, and post mortem cross-sectional scanning electron microscopy (SEM) measurements evidences the electrochemo-mechanically compliant microstructure of FCG75, which results in a high discharge capacity of 194 mA h g^{-1} with a high initial CE of 85% between 3.0 and 4.3 V (vs Li/Li+) at 0.1 C (0.17 mA cm^{-2}) and 30 °C, and a stable cycling retention of 79.1% after 200 cycles cycled at 0.5 C. This promising performance of FCG75 is in stark contrast to that of NCA80

(discharge capacity of 156 mA h g^{-1}, initial CE of 71%, and cycling retention of 46.9%), which stems from the severe disintegration of microstructures.

2. Results and Discussion

NCA80 and FCG75 without surface coatings and structural doping were selected as model cathode materials because they have a distinct microstructural difference while sharing common features in terms of the Ni contents, the secondary particle morphologies and size distributions (Figure S2, Supporting Information), the surface areas (Figure S3, Supporting Information), and the lattice structures (Figure S4 and Table S3, Supporting Information). Inductively coupled plasma optical emission spectroscopy (ICP-OES) was employed to confirm the average chemical composition of NCA80 and FCG75 cathode materials ($Li[Ni_{0.798}Co_{0.160}Al_{0.042}]O_2$ and $Li[Ni_{0.751}Co_{0.101}Mn_{0.148}]O_2$, respectively). In the commercial-grade NCA80, primary particles are randomly oriented, forming overall spherical secondary particles (**Figure 1**a). In contrast, in FCG75, the high-aspect-ratio primary particles are radially oriented in the outward *a-b* plane direction (Figure 1b), which is a unique feature derived by tailoring the concentration-gradient of NCM particles.[54–56] The electron probe micro-analyzer (EPMA) composition profile for the cross-sectioned FCG75 particle indicates the concentration of Ni in the core is higher than at the surface, while the concentration of Mn at the surface is higher than in the core (Figure S5, Supporting Information). This was demonstrated to maximize the capacity without the loss of thermal and/or cycling stability when applied to LE-based advanced LIBs.[54–56]

The electrochemical performances of the NCA80 and FCG75 electrodes cycled between 3.0 and 4.3 V (vs Li/Li+) at 30 °C are compared between LE cells and all-solid-state cells in Figure 1c–f. For the LE cells, the first charge capacities at 0.1 C are almost identical for the FCG75 and NCA80 electrodes (217–219 mA h g^{-1}), and the FCG75 electrode shows a higher first discharge capacity (212 mA h g^{-1}) than that for the NCA80 electrode (204 mA h g^{-1}) despite the lower Ni content. This could be rationalized by the more stable interfaces as well as the rod-shaped texture, which facilitates Li+ diffusion.[54–56] For all-solid-state cells, the first charge capacities (229 and 219 mA h g^{-1} for FCG75 and NCA80, respectively) are roughly comparable to those of LE cells. Strikingly, the first discharge capacities for FCG75 and NCA80 show a huge difference, with values of 194 and 156 mA h g^{-1} respectively, which translate into CEs of 84.9% and 71.2%. This result seems to be associated with the higher polarization of NCA80 than FCG75 in the discharge voltage profiles (Figure 1d). Consistently, the overall rate performances follow the trend in the first discharge capacities (Figure 1e,f), the slightly different performances of FCG75 and NCA80 in LE cells lead to a dramatic difference in all-solid-state cells.

Figure 1g presents the cycling stability results of NCA80 and FCG75 electrodes in all-solid-state half-cells cycled at 0.5 C by constant current and constant voltage (CCCV) mode for charge with a limiting current of 0.05 C at 30 °C. The capacity retention for NCA80 after 200 cycles is 46.9%, which is in sharp
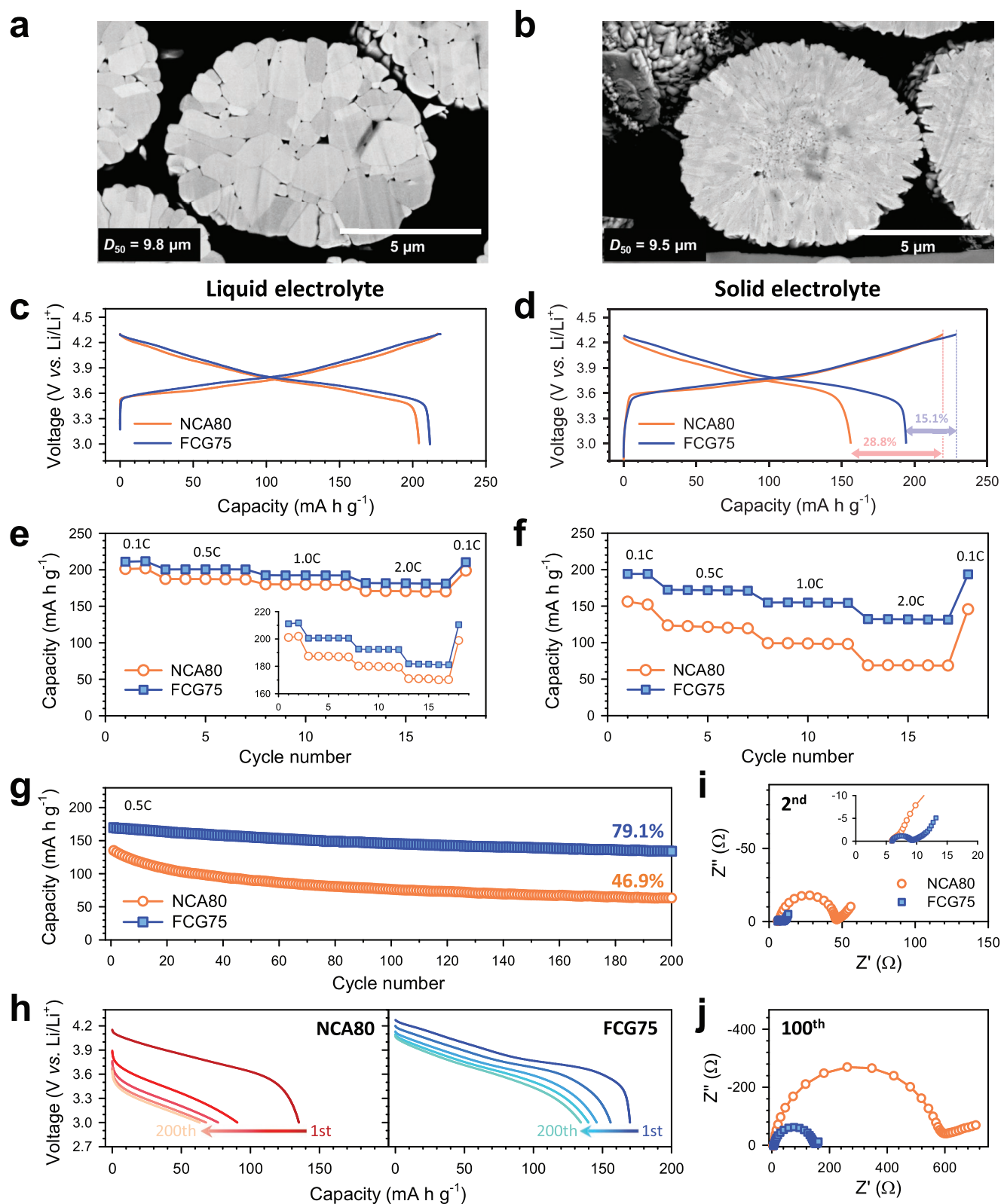
Figure 1. Comparative electrochemical characterization of NCA80 and FCG75 in liquid electrolyte (LE) cells and all-solid-state half-cells at 30 °C. Cross-sectional SEM images of a) NCA80 and b) FCG75 particles. The average particle sizes are also shown in each panel. First-cycle charge–discharge voltage profiles for c) LE cells (NCA80/Li and FCG75/Li), d) all-solid-state cells (NCA80/Li-In and FCG75/Li-In), and e,f) their corresponding rate performances. g) Cycling performances at 0.5 C and h) the corresponding discharge voltage profiles at different cycle numbers (1, 50, 100, 150, 200) for NCA80/Li-In and FCG75/Li-In all-solid-state cells. Nyquist plots for NCA80/Li-In and FCG75/Li-In all-solid-state cells at i) 2nd and j) 100th cycles. The cells discharged to 3.8 V (vs Li/Li$^+$) at each cycle were subjected to the electrochemical impedance spectroscopy (EIS) measurements.

ADVANCED
SCIENCE NEWS
www.advancedsciencenews.com

ADVANCED
ENERGY
MATERIALS
www.advenergymat.de

contrast to the unprecedentedly high value of 79.1% for FCG75. The growth of nominal voltage polarization between charge and discharge, which is severe at initial cycles (≤50–100 cycles), is more pronounced for NCA80 than for FCG75 (Figure S6, Supporting Information). Moreover, the discharge voltage profiles at different cycles shown in Figure 1h clearly display much slower development of polarization for FCG75 than for NCA80. The electrochemical impedance spectroscopy (EIS) signals measured in the charged state at 3.8 V (vs Li/Li+) at the 1st and 100th cycles are shown as Nyquist plots in which depressed semicircles are followed by Warburg tails (Figure 1i,j and Table S4, Supporting Information). The experimental data fitted with the equivalent circuit model (Figure S7, Supporting Information) indicate that the resistances of both the NCA80 and FCG75 SE layers remain constant (R_1 + R_2 = 6–7 Ω) regardless of the number of cycles. These resistances are assigned as the grain and grain boundary resistances in the SE layer, respectively.[24,46] The R_3 values are attributed to interfacial resistance, and that for NCA80 (39.6 Ω) dramatically increases at the first cycle, compared to that for FCG75 (2.6 Ω). Moreover, the increase in the R_3 values after 100 cycles is much larger for NCA80 (598 Ω) than for FCG75 (146 Ω).[57,58]

In short, the dramatic performance difference between FCG75 and NCA80 in all-solid-state cells, compared to those in the conventional LE cells raises an intriguing question.

The first charge capacities of NCM electrodes in all-solid-state cells are attributed mainly to the deintercalation of Li+ ions from NCM lattices. However, the contribution of any side reactions, such as oxidative decomposition of SEs, should also be considered. In order to determine whether this contribution varies largely between NCA80 and FCG75 in all-solid-state cells, a control experiment was carried out. After the all-solid-state cells were charged at normal conditions (0.1 C and 30 °C), they were subjected to discharge at a lowered C-rate of 0.05 C by CCCV mode (limiting current of 0.01 C) and at an elevated temperature of 70 °C at which all kinetic factors are boosted (**Figure 2**a). While FCG75 shows a slight increase of only 6 mA h g−1 in the discharge capacity compared to the case for normal discharge (from 194 (Figure 1d) to 200 mA h g−1), the increase in the discharge capacity for NCA80 is as high as 31 mA h g−1 (from 156 to 187 mA h g−1, the values are summarized in Table S5, Supporting Information). Accordingly, the CE values for NCA80 reach 85.5% which is comparable to that for FCG75 (86.8%). This result clearly indicates that the much lower first discharge capacity or CE value of NCA80 relative to that for FCG75 in Figure 1d is not due to different state of charges (SOC) caused
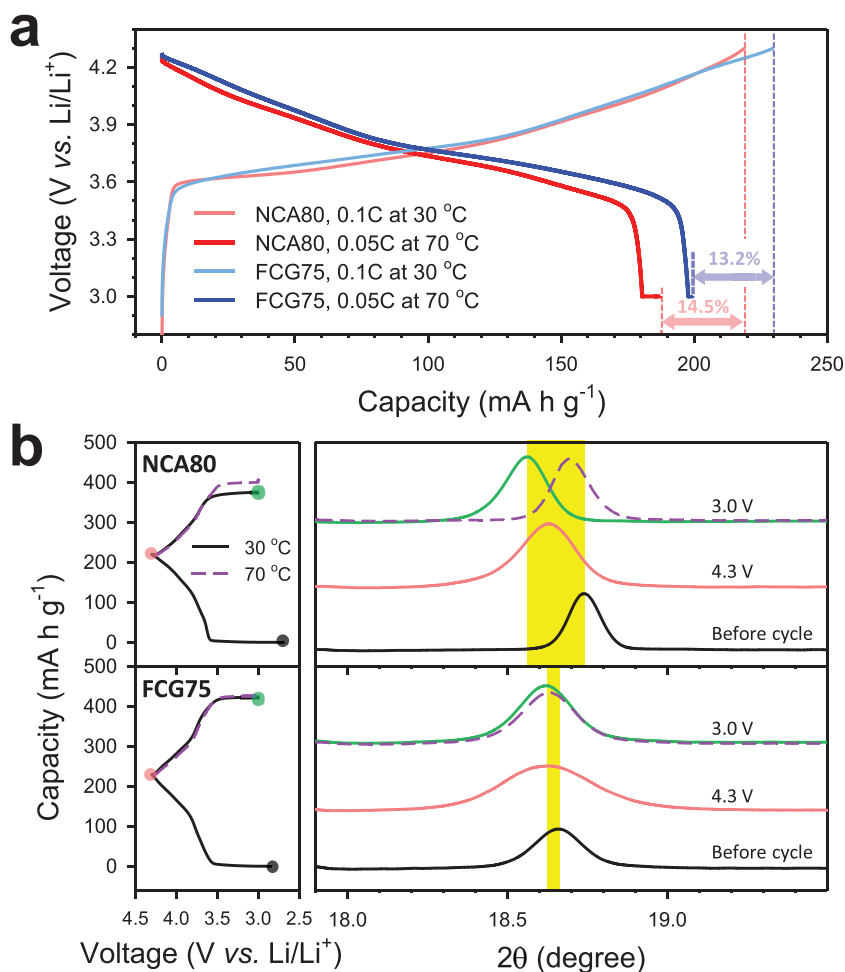

Figure 2. a) First-cycle charge–discharge voltage profiles of NCA80 and FCG75 in all-solid-state cells charged at 0.1 C and 30 °C and discharged at 0.05 C with a limiting current of 0.01 C at 70 °C. b) Ex situ XRD patterns showing (003) peaks for NCA80 and FCG75 at different SOCs for the electrodes in all-solid-state cells at 30 or 70 °C. The corresponding charge–discharge voltage profiles at 0.1 C are displayed in the left panel. The discharge voltage profiles at 0.05 C and 70 °C and the resulting XRD patterns are shown in dashed lines. Note the larger peak shift to negative angle after discharge of NCA80 relative to that of FCG75, compared with the peaks for the pristine samples when discharged at 30 °C. Also, note the dramatic recovery of the peak position for NCA80 when discharged at 70 °C, compared with the pristine sample. The peak position and FWHM values for the ex situ XRD data are summarized in Table S6, Supporting Information.

by different amounts of side reactions during the first charge. The ex situ XRD results for all-solid-state cells at three different SOCs during the first cycle at 0.1 C and 30 °C (or charge at 0.1 C and 30 °C, followed by discharge at 0.05 C and 70 °C, denoted dashed lines) are shown in Figure 2b. It is noted that the position for the (003) peak after discharge to 3.0 V (vs Li/Li+) at 30 °C is much more negatively shifted for NCA80 than for FCG75, compared to each original position prior to cycling. This negative peak shift for NCA80 is dramatically alleviated for the case of discharge at 70 °C at which the kinetics are accelerated. These results reflect that the first discharge in NCA80 (at 30 °C) is far from full Li+ intercalation into the lattice,[25] which should originate from the slow kinetics as evidenced by the control experiment in Figure 2a. Further discussion will be presented later.
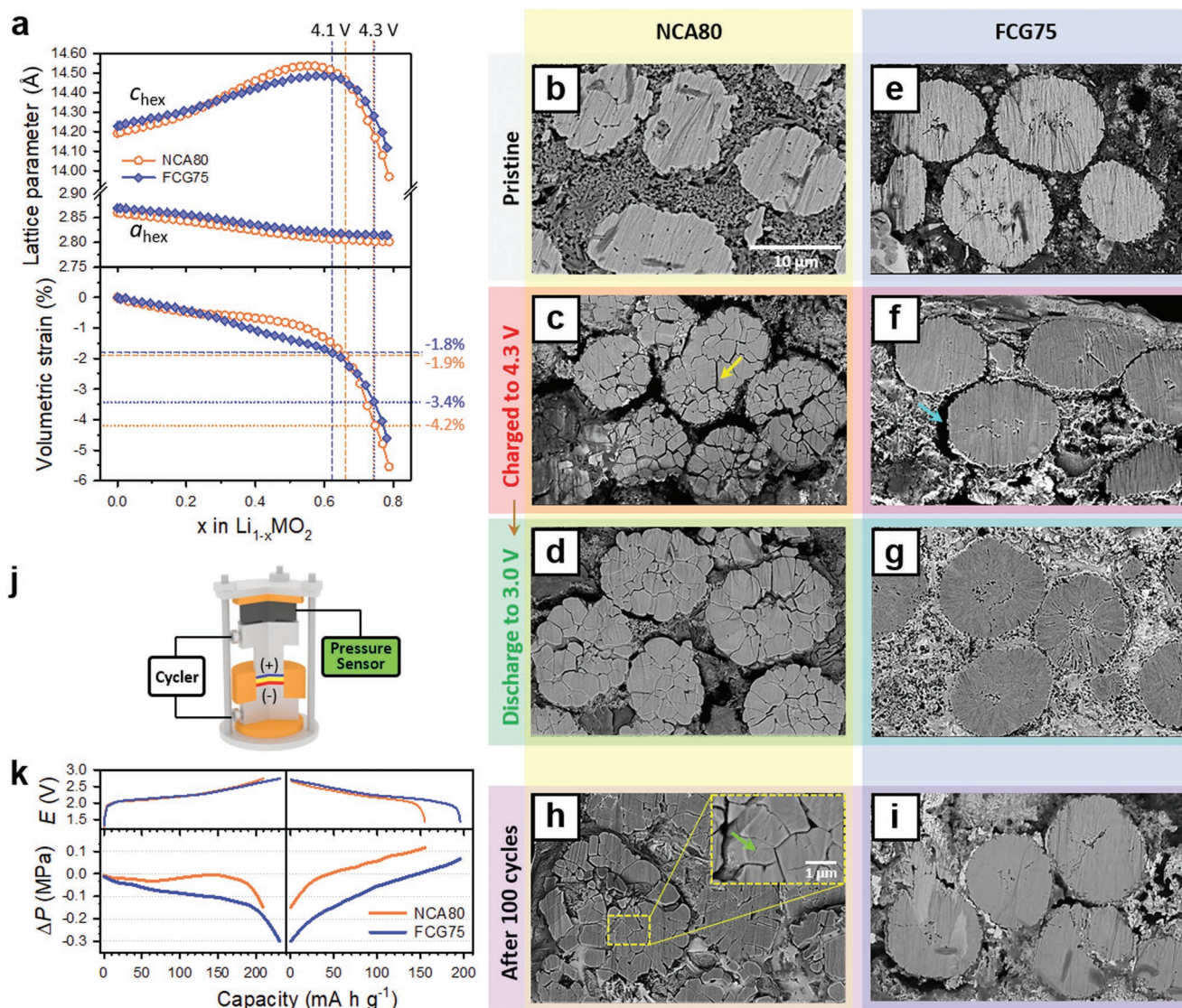
**ADVANCED
SCIENCE NEWS**

www.advancedsciencenews.com

**ADVANCED
ENERGY
MATERIALS**

www.advenergymat.de

Figure 3. Electrochemo-mechanical characterization of NCA80 and FCG75 electrodes for all-solid-state cells. a) Lattice parameters and volumetric strain (($V_{final} - V_{initial})/V_{initial}$) for NCA80 and FCG75 as a function of SOC (x in $Li_{1-x}MO_2$), obtained by the analysis of in situ XRD measurements of LE cells. The corresponding in situ XRD data are shown in Figure S8, Supporting Information. Cross-sectional SEM images of NCA80 electrodes b) before cycling and after c) first charge to 4.3 V (vs Li/Li$^+$) and d) the subsequent discharge to 3.0 V (vs Li/Li$^+$). e–g) The corresponding images for FCG75 electrodes. Cross-sectional SEM images of h) NCA80 and i) FCG75 electrodes after 100 cycles. j) Schematic illustration of pressure monitoring NCM/Li$_4$Ti$_5$O$_{12}$ all-solid-state cells and k) the corresponding operando electrochemical pressiometry profiles for FCG75 and NCA80 during first charge–discharge at 0.1 C and 30 °C.

To sum the results, the huge difference in the performances of FCG75 and NCA80 in all-solid-state cells at initial cycles is associated with the different overpotential, which is not attributed to any side reaction effect. This leads us to the indispensable consideration of an electrochemo-mechanical effect. The volumetric strains in LE cells with NCA80 and FCG75 at a cutoff voltage of 4.3 V (vs Li/Li$^+$) were found to be −4.2% and −3.4%, respectively (**Figure 3**a), from analysis of the in situ XRD results (Figure S8, Supporting Information). The slopes of the volumetric strains become noticeably steeper (and the slope of the lattice parameter c_{hex} changes drastically) above ≈4.1 V (vs Li/Li$^+$), at which the deleterious H2–H3 phase transition may occur.[43,51,52,59,60] Up to 4.1 V (vs Li/Li$^+$), the volumetric strains

for NCA80 and FCG75 are only −1.9% and −1.8%, respectively. Accordingly, in contrast to the different electrochemical performances at the cutoff voltage of 4.3 V (vs Li/Li$^+$) (Figure 1g), both NCA80 and FCG75 show comparably good cycling stabilities when the voltage is restricted to 4.1 V (vs Li/Li$^+$) (Figure S9, Supporting Information, shows cycling retentions of 88.6 and 88.2% for NCA80 and FCG75, respectively, after 200 cycles), suggesting the importance of the electrochemo-mechanical effect.

In order to visualize the electrochemo-mechanical evolution of electrode microstructures, cross-sectional SEM images of the NCA80 and FCG75 electrodes in all-solid-state cells were obtained before cycling (Figure 3b,e) and after the first charge

ADVANCED
SCIENCE NEWS
www.advancedsciencenews.com

ADVANCED
ENERGY
MATERIALS
www.advenergymat.de

to 4.3 V (vs Li/Li$^+$) (Figure 3c,f) and the subsequent discharge to 3.0 V (vs Li/Li$^+$) (Figure 3d,g). For NCA80 particles, even after the first charge, formation of intergranular cracks as well as void spaces between NCA80 and SEs are evident (Figure 3c, indicated by the yellow arrow). This result is explained by the overall shrinkage of the lattice volume by ≈4.2% (Figure 2a). Upon first discharge, the formed cracks still remain (Figure 3d).

For the FCG75 electrodes, the detachment of SEs from the active material particles is also observed after the first charge (Figure 3f, indicated by the sky-blue arrow), which is because of the volumetric shrinkage associated with the H2-H3 phase transition during charging above ≈4.1 V (vs Li/Li$^+$). However, the void space between the SE and cathode particles is observed to be narrower for FCG75 than for NCA80, which is explained by the smaller volumetric shrinkage for FCG75 compared to that for NCA80. Importantly, no cracks inside the FCG75 particles are observed. Even after the subsequent discharge, the structure of the secondary particles of FCG75 remains intact (Figure 3g). Moreover, the void spaces between active material particles and SEs disappear.[61,62] After 100 cycles, the difference in mechanical integrity between the NCA80 and FCG75 electrodes becomes more amplified (Figure 3h,i). For sampling of the NCA80 electrode after 100 cycles, instead of an electrode pellet specimen, finely shattered particles were collected from the electrode layers, reflecting the severe disintegration of the entire structure (Figure S10, Supporting Information). In contrast, collecting a fractured electrode pellet specimen was possible for the FCG75 electrode after 100 cycles (Figure S11, Supporting Information). For NCA80, the secondary particles were fully disintegrated into primary particles after 100 cycles (Figure 3h). Surprisingly, few fine cracks were observed for FCG75, even after 100 cycles (Figure 3i), manifesting its mechanically compliant nature.

The appearance of distinct cracks, even after the first discharge, in NCA80 for all-solid-state cells (Figure 3d) is not common for Ni-rich cathode materials in LIBs using LEs.[44,52,63] Although the uniaxially applied pressure is released after the cold-pressing process, any stresses may remain locally due to elastic and plastic deformation of the SEs.[48,64] Importantly, the cells are operated under external uniaxial pressure. It is thus suggested that the aforementioned factors could facilitate the formation of cracks which must be triggered by the shrinkage of primary particles. The anisotropic volumetric shrinkage and the randomly oriented crystal directions for each primary particle are likely to have synergistic effects on accelerating the formation of severe cracks during the initial charge process (Figure 3c).[43,51,52,60] In the subsequent discharge process, the aforementioned inhomogeneity of the electrode pressure renders the dislocated primary particles not being relocated to the original position despite the volumetric expansion, leading to severe disintegration. In contrast, the radial alignment of high-aspect-ratio primary particles can effectively accommodate reversible volume changes without suffering from the formation of intergranular cracks.[43,51,52,56]

Noting that the formation of cracks indicates the creation of void spaces, operando electrochemical pressiometry measurements were carried out for NCA80 and FCG75 in all-solid-state cells employing zero-strain Li$_4$Ti$_5$O$_{12}$ as the anode (or counter electrode) (Figure 3j,k). Based on the theoretical calculation using the volumetric strains obtained from the in situ XRD data (Figure 3a), it may be expected that the pressure changes for NCA80 are larger than those for FCG75 during charge–discharge (see the Supporting Information for details).[48] However, the measured pressure decrease for NCA80 after the first charge is shown to be even lower (–0.15 MPa) than that for FCG75 (–0.30 MPa). This result directly indicates the formation of void spaces (or cracks) in NCA80, agreeing well with the severe intergranular cracks observed only in NCA80 (Figure 3c). The pressure increases for both NCA80 and FCG75 upon discharge are also consistent with expansion of the lattice volume (Figure 3a). At the end of discharge, the overall pressure changes are positive for both NCA80 and FCG75. The positive pressure change even for FCG75 could imply incomplete recovery of the ionic contacts between FCG75 and Li$_6$PS$_5$Cl (SE), rather than the disintegration of the active material particles. Importantly, the pressure for NCA80 after one cycle is higher than that for FCG75, although less Li$^+$ ions are inserted in the lattice of NCA80 than FCG75, which is also in good agreement with the severe mechanical degradation of NCA80 electrodes observed in the SEM image (Figure 3d).

Mechanical degradation by repeated cycling causes the ionic contacts of primary particles, especially in the core, to be loosened and/or lost, which could result in incompleteness and heterogeneity in discharge (or lithiation). This is supported by the large negative shift of the (003) peak for NCA80 after discharge at 30 °C in the ex situ XRD result, which is in sharp contrast to the marginal shift for FCG75 (Figure 2b). Moreover, for NCA80, the more broadened (003) peak after discharge, compared to that of the pristine electrode, likely indicates the presence of primary particles with more varied SOCs, which is also indicative of electrochemo-mechanically driven deteriorated ionic contacts. (see Table S6 and Figure S12, Supporting Information, for details).

It is now evident that the electrochemo-mechanical effect dominates the huge difference in the electrochemical performances of all-solid-state cells employing NCA80 and FCG75. Even though the effect of interfacial (electro)chemical stability (or the side reaction) between NCA80 (or FCG75) and Li$_6$PS$_5$Cl is shown to be non-critical, at least at the initial cycle, it may not be negligible with regards to long-term stability. Thus, its assessment was carried out by ex situ transmission electron microscopy (TEM) and X-ray photoelectron spectroscopy (XPS) analyses of the electrodes collected from all-solid-state cells cycled 100 times (**Figures 4** and **5**).

The results of the surface and core regions of the cathode material particles are shown in Figure 4a,b for NCA80 and Figure 4c,d for FCG75. Mosaic scanning TEM images of cycled electrodes are provided in Figure S13, Supporting Information. For both NCA80 and FCG75, the surface regions that are in contact with SEs show distinctly different textured surface layers (denoted as "i"), compared to the inner regions (denoted as "ii") (Figure 4a,c). The corresponding selected area electron diffraction (SAED) patterns (for the region "i") reflect the NiO-like rock-salt structure with space group $Fm\overline{3}m$, which should be converted from the original layered structure ($R\overline{3}m$). In contrast, the core regions (Figure 4b,d) show homogeneous lattice fringes and the SAED patterns indicate a layered structure with the space group $R\overline{3}m$ ("ii"). It is well known that in conventional
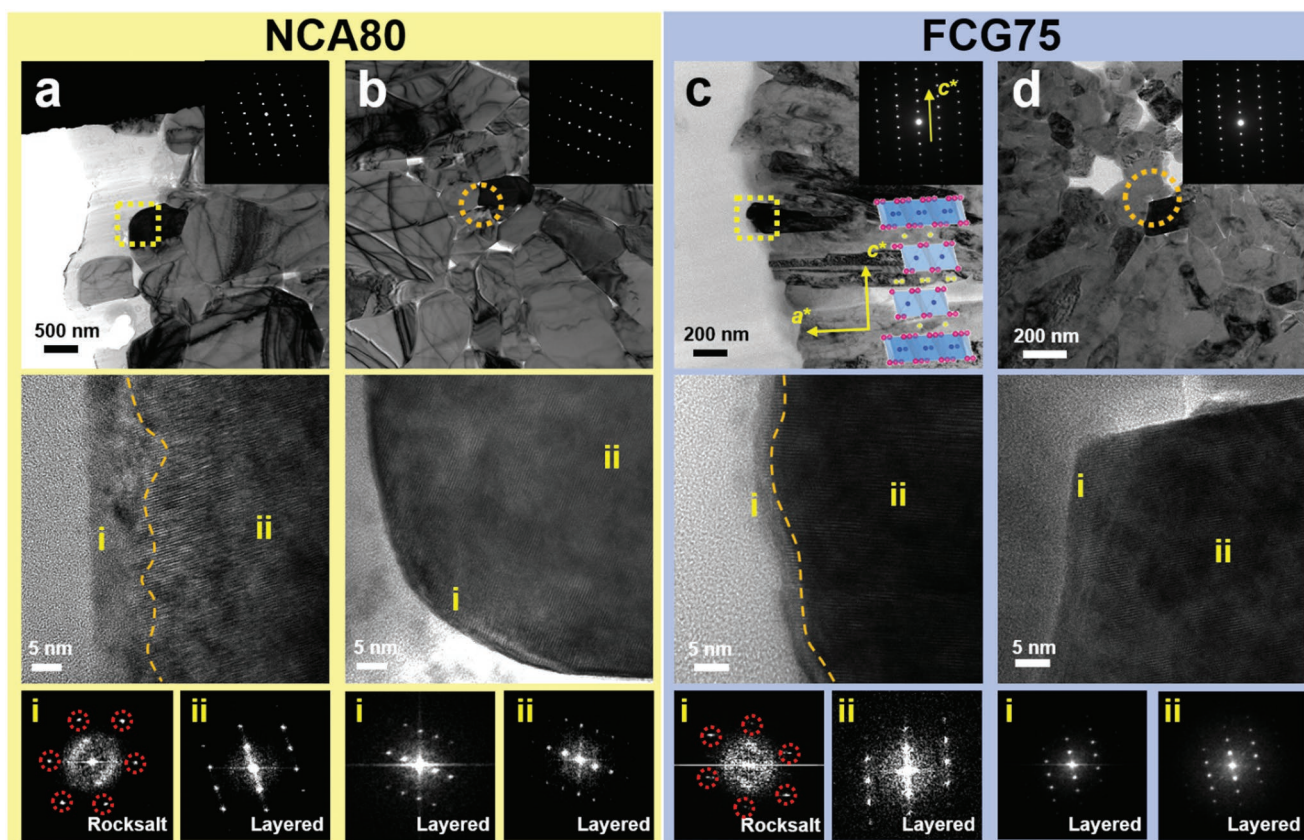
Figure 4. Ex situ TEM results of NCA80 and FCG75 for all-solid-state cells cycled 100 times. Low and high magnification ex situ TEM images for a) surface and b) core regions of the secondary particle for NCA80 and their corresponding SAED patterns. c,d) The corresponding results for FCG75. Structural information deduced from the SAED patterns is also shown in each panel.

LIBs the formation of a rock-salt phase in which Li$^+$ transport is impeded is associated with the reduction of unstable Ni^{4+} to Ni^{2+} facilitated by the decomposition of LEs.[51,65,66] Based on the observed formation of rock-salt phase only in the region in contact with the SE (Li$_6$PS$_5$Cl), it is suggested that, similar to the case of LE cells, the reduction of Ni^{4+} to Ni^{2+} would induce

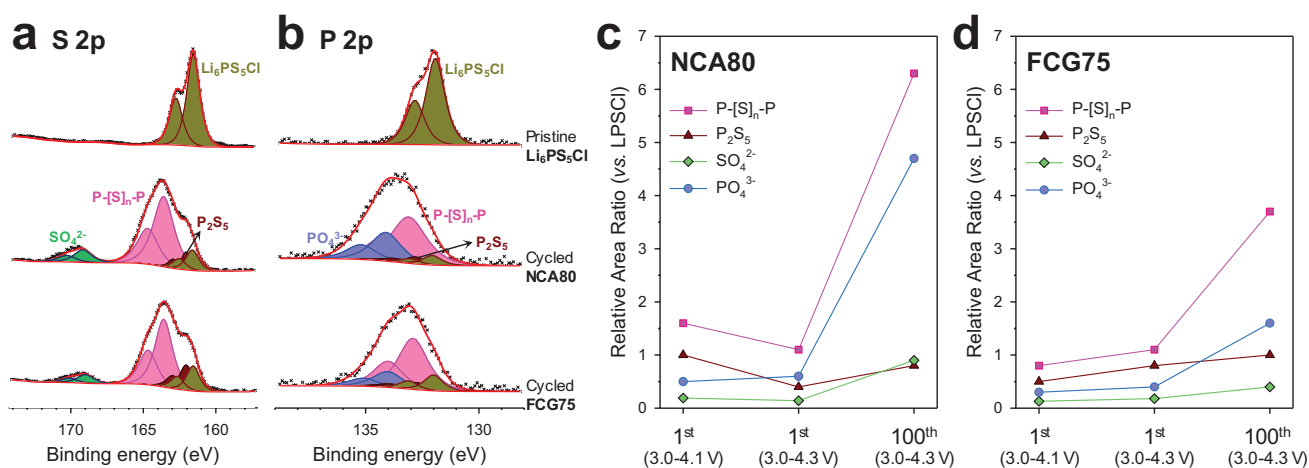**Figure 5.** Ex situ XPS results of NCA80 and FCG75 for all-solid-state cells. a) S 2p and b) P 2p XPS signals for pristine Li$_6$PS$_5$Cl and electrodes cycled for 100 times. The relative area ratio for the Li$_6$PS$_5$Cl-derived oxidized species for c) NCA80 and d) FCG75 after different cycle numbers (1 or 100) and upper cutoff voltages (4.1 or 4.3 V vs Li/Li$^+$). Note that all the cycled electrodes were discharged to 3.0 V (vs Li/Li$^+$) prior to the measurements regardless of the upper cutoff voltages. The ex situ XPS data after one cycle and the fitted results are provided in Figure S15 and Table S7, Supporting Information, respectively.

the oxidation of Li_6PS_5Cl along with the phase transition from a layered structure to a rock-salt structure.

This rationale is successfully supported by the corresponding S 2p and P 2p ex situ XPS results (for the electrodes after 100 cycles, Figure 5a,b). After cycling, the evolution of oxidized species of SO_4^{2-}, PO_4^{3-}, bridging sulfur (P-$[S]_n$-P), and P_2S_5, derived from Li_6PS_5Cl is observed, which is in agreement with previous results.[33,67] Both NCA80 and FCG75 show slight positive shifts in Ni 2p XPS peaks after cycling (Figure S14, Supporting Information), indicating the existence of Ni with the oxidation states of >2+. Comparison of their peak shapes shows that the contribution at higher binding energies is likely larger for NCA80 than for FCG75. This result may also be in line with the kinetically driven incomplete lithiation (or reduction) after discharge for NCA80, shown in Figure 2. The ex situ XPS signals for Co and Mn remain unchanged after cycling (Figure S14, Supporting Information), which is in contrast to the formation of detrimental Co_3S_4 for $LiCoO_2$ in ASLBs cycled just once in our previous result.[24] This discrepancy may be an interesting subject for theoretical calculations,[29,32,35] and could be responsible for the decent electrochemical performances of FCG75 despite the absence of any protective coatings.

In the ex situ TEM images (for the electrodes after 100 cycles, Figure 4a,c), the thickness of the insulating rock-salt layer is smaller for FCG75 (≈3 nm) than for NCA80 (13–15 nm), which can be explained by the lower amount of Ni on the surface of FCG75 (≈70%) than of NCA80 (80%) (Figure S5, Supporting Information). The relative XPS signal area ratios for Li_6PS_5Cl-derived oxidized species with respect to those for Li_6PS_5Cl are compared for the electrodes cycled once (with the upper cutoff voltages of 4.3 or 4.1 V vs Li/Li^+) and for 100 times in Figure 5c,d. The S 2p and P 2p XPS data for the electrodes cycled once are provided in Figure S15, Supporting Information. Consistent with the ex situ TEM results, the ex situ XPS results also indicate larger amount of Li_6PS_5Cl-derived oxidized species for NCA80 than for FCG75 after 100 cycles (Figure 5c,d and Table S7, Supporting Information). In contrast, the relative amounts of Li_6PS_5Cl-derived oxidized species do not show significant differences between NCA80 and FCG75 after the initial cycle. Thus, the contribution of the interfacial electrochemical stability effect for all-solid-state cells could be marginal to the difference in the reversibility at the initial cycle but could not be neglected to the difference in the long-term cycling stability. It is also noted that the variation of the upper cutoff voltages (4.1 or 4.3 V vs Li/Li^+) does not result in significant difference in the amounts of the oxidized species. This result cannot explain the electrochemical behaviors of all-solid-state cells (i.e., the similar performances between NCA80 and FCG75 in the voltage range of 3.0–4.1 V (vs Li/Li^+) (Figure S9, Supporting Information) but the largely different performances in the voltage range of 3.0–4.3 V (vs Li/Li^+) (Figure 1)), strongly supporting the dominance of the electrochemo-mechanical effects.

Our results for FCG75 in ASLBs are promising and provide important insights on the design principle for further developments. Although FCG75 itself is electrochemo-mechanically compliant, the ionic contacts with the SEs are loosened upon repeated cycling. Introduction of Li^+ conductive soft materials could be one of the strategies to address this issue. In our previous work, tailoring the NCM electrodes for ASLBs using slurry-fabricable Li^+ conductive polymeric binders could significantly improve the electrochemical performances, due to the enhanced ionic contacts at the NCM/SE interfaces.[25] It is also suggested that the Li^+ conductive polymeric binders infiltrated into the intergranular cracks, enabling the utilization of the electrochemo-mechanically disintegrated inner grains, which was overlooked. Additionally, it should be noted that the results herein for FCG75 were obtained with the bare sample. Further improvement in performance could be possible by intensive interfacial engineering, such as the application of protective coatings[16,24,32,37–39] and/or the development of advanced SE materials with improved oxidation stability,[68] which will be our next mission in future.

Finally, the promising performances of ASLBs using the electrochemo-mechanically compliant micro-structured FCG75 were compared with the previous results of ASLBs using other NCM electrodes in **Figure 6**a,b and Table S1, Supporting Information. The former possesses the highest capacity and the best cycling stability. Furthermore, the FCG cathodes were combined with Li metal anodes and cycled between 3.0 and 4.3 V at 0.2 C and 30 °C. Their first two-cycle charge–discharge voltage profiles and the corresponding cycling stability are displayed in Figures 6c and 6b, respectively. The FCG75/Li ASLBs show a high reversible capacity of 180 mA h g^{-1} and a promising cycling retention of 84.2% after 100 cycles. Furthermore, FCG75/Li ASLBs cycled at 70 °C and 0.05 C show a high discharge capacity of 207 mA h g^{-1}, corresponding to 3.2 mA h cm^{-2} (Figure 6d), which translates into an energy density of 88.2 W h kg_{cell}^{-1} based on the total weight, including the composite electrodes, SE layer, and current collectors. By reducing the SE layer thickness to 50 μm or less, the energy density could be increased to 393 W h kg_{cell}^{-1}, thereby reaching the target sufficiently for safe and long-range (over ≈630 km) electrified vehicles.[50,69]

3. Conclusion

In summary, complementary analysis via an arsenal of electrochemical, ex situ and in situ XRD, operando electrochemical pressiometry, post-mortem SEM, ex situ TEM, and ex situ XPS measurements successfully revealed the effects of electrochemo-mechanically-driven microstructural and interfacial evolutions on the electrochemical performances of Ni-rich cathode materials in ASLBs, which are illustrated in **Figure 7**. The anisotropic volume changes of randomly oriented primary particles in NCA80 collectively caused the severe disintegration of secondary particles, even at the initial cycle. In contrast to the conventional LIBs, in which LEs can wet any exposed grain surfaces, the SEs cannot access the ionically disrupted inner grains, which explains the much poorer electrochemical performances of NCA80 in all-solid-state cells compared to those in LE cells. In sharp contrast, the radially aligned high-aspect-ratio grains in FCG75 can reversibly accommodate volume changes without mechanical degradation. This distinctly different microstructural evolution was responsible for the huge difference in the electrochemical performances of ASLBs. Moreover, the lower occurrence of side reaction at NCM/Li_6PS_5Cl interfaces for FCG75 than for NCA80 owing to the lower Ni content
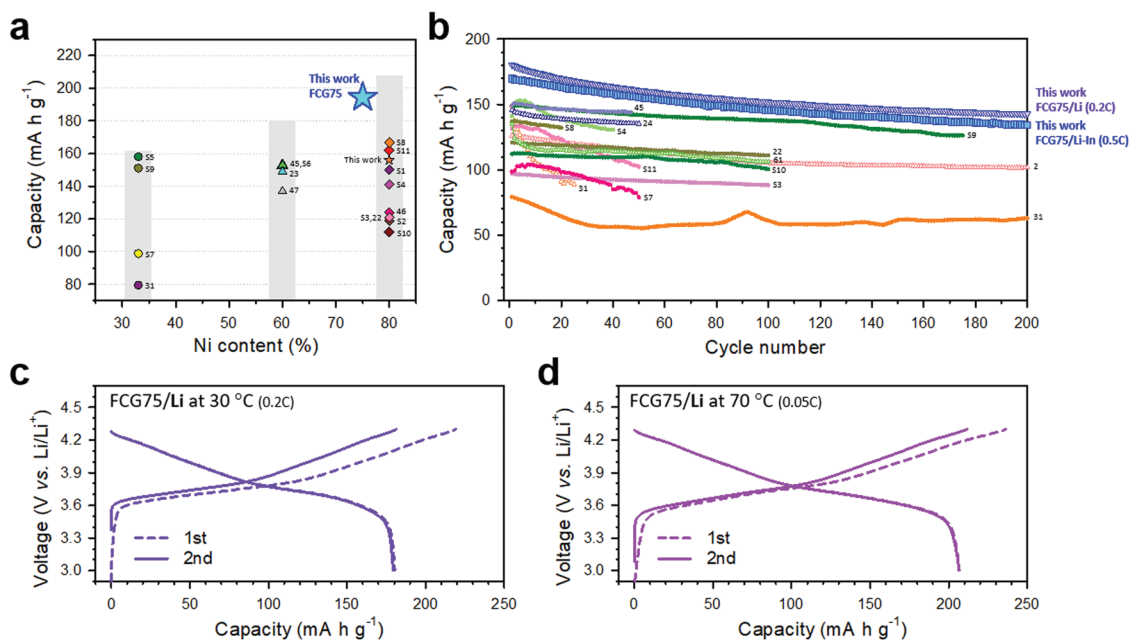
Figure 6. Highlights of the performance of FCG75 for ASLBs. Comparison of a) first-cycle discharge capacity and b) cycling performance with those of various NCM electrodes for ASLBs at room temperature, varied by Ni content. The vertical gray bars in (a) indicate the capacities of the LE cells. First two-cycle charge–discharge voltage profiles for FCG75/Li ASLBs c) at 30 °C and d) at 70 °C. The cycling performance of FCG75/Li ASLBs at 30 °C is also shown in (b).
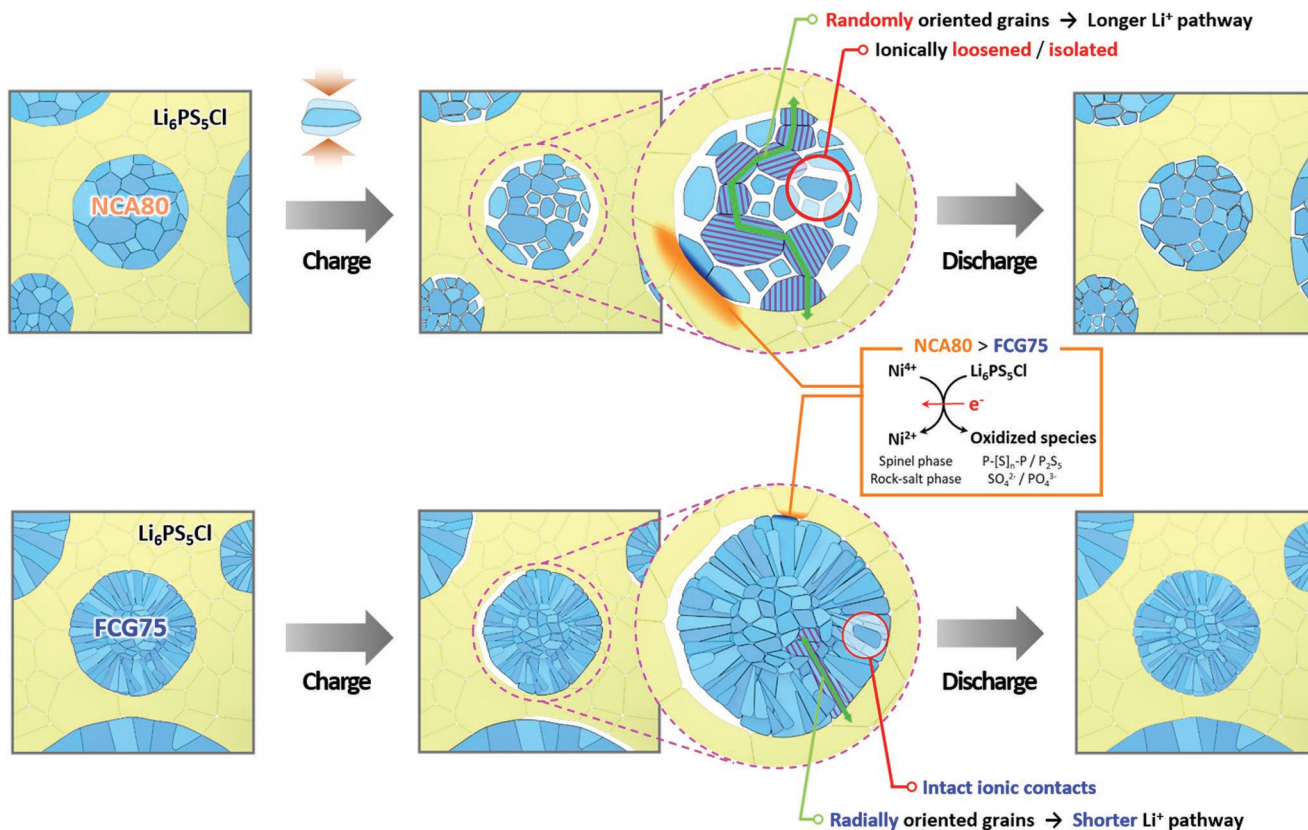

Figure 7. Schematic illustrating the different microstructural and interfacial evolutions in the NCA80 and FCG75 electrodes in all-solid-state cells.

ADVANCED
SCIENCE NEWS
www.advancedsciencenews.com

ADVANCED
ENERGY
MATERIALS
www.advenergymat.de

on the surfaces of FCG75 than those of NCA80 contributed to the corresponding better long-term cycling stability. It must be emphasized that FCG75 in all-solid-state cells exhibited the best performance to date (a high reversible capacity reaching ≈200 mA h g^{-1} at 0.1 C and 30 °C, a high initial CE of 84.9%, and a good cycling retention of 79.1% at 0.5 C after 200 cycles). Finally, the excellent reversibility of FCG75/Li ASLBs was demonstrated at 30 °C and at 70 °C. Our results shed light on the design principle for cathode materials and interfaces customized for practical all-solid-state technologies for safe and long-range battery-driven electric vehicles.

4. Experimental Section

Materials Synthesis: The spherical FCG [Ni$_{0.75}$Co$_{0.10}$Mn$_{0.15}$](OH)$_2$ precursors were synthesized via the coprecipitation method. A Ni-poor aqueous solution (Ni:Co:Mn = 0.645:0.149:0.206 in molar ratio) of NiSO$_4$·6H$_2$O, CoSO$_4$·7H$_2$O, and MnSO$_4$·H$_2$O was pumped into a Ni-rich (Ni:Co:Mn = 1.0:0:0.0 in molar ratio) solution. The homogeneously mixed solution was fed into a reactor (17 L) filled with a solution of NH$_4$OH and NaOH under an inert atmosphere. Spherical Ni(OH)$_2$ particles were formed first, after which nickel–cobalt–manganese hydroxides of various compositions slowly accumulated on the surfaces of the pre-formed particles, resulting in radial concentration gradients of Ni, Co, and Mn in each particle. Powders were obtained by filtering, washing, and overnight drying at 110 °C. To obtain FCG Li[Ni$_{0.75}$Co$_{0.10}$Mn$_{0.15}$]O$_2$, the FCG precursor with an average composition of [Ni$_{0.75}$Co$_{0.10}$Mn$_{0.15}$](OH)$_2$ was mixed with LiOH·H$_2$O (Li:(Ni+Co+Mn) = 1.01:1 in molar ratio) and fired at 790 °C for 10 h under flowing O$_2$. Spherical NC [Ni$_{0.84}$Co$_{0.16}$](OH)$_2$ precursor without a concentration gradient and a rod-shape morphology was synthesized via the co-precipitation method with 2.0 M of NiSO$_4$·6H$_2$O and CoSO$_4$·7H$_2$O aqueous solution (Ni:Co = 84:16 molar ratio) as the starting materials. A homogeneously mixed solution was fed into a reactor (17 L) filled with a solution of deionized water, NH$_4$OH (aq), and NaOH under an inert atmosphere. Concurrently, 4 M NaOH (aq) (molar ratio of NaOH to transition metal = 2.0) and an NH$_4$OH chelating agent (aq) (molar ratio of NH$_4$OH to transition metal = 1.2) were pumped separately into the reactor. The final precursor powders were obtained by filtration, washing with deionized water and overnight drying under vacuum at 110 °C. To obtain Li[Ni$_{0.80}$Co$_{0.16}$Al$_{0.04}$]O$_2$, the precursor [Ni$_{0.84}$Co$_{0.16}$](OH)$_2$ was mixed with LiOH·H$_2$O and Al(OH)$_3$·3H$_2$O (Li:Al:(Ni+Co) = 1.01:0.04:0.96 in molar ratio) and fired at 770 °C for 10 h under flowing O$_2$. For Synthesis of Li$_6$PS$_5$Cl, stoichiometric amounts of Li$_2$S (99.9%, Alfa Aesar), P$_2$S$_5$ (99%, Sigma-Aldrich) and LiCl (99.99%, Sigma-Aldrich) were mixed at 600 rpm for 10 h with ZrO$_2$ balls using Pulverisette 7 PL (Fritsch GmbH). The ball-milled powders were subjected to heat-treatment at 550 °C for 5 h under an Ar atmosphere.

Materials Characterization: The chemical compositions of the prepared cathode active material powders were determined by ICP-OES (OPTIMA 8300, Perkin Elmer). To confirm the localized composition of NCA80 and FCG75, cross-sectioned particles were prepared by embedding the particles in epoxy and grinding them flat. The elemental line scans of the polished NCA80 and FCG75 were obtained by EPMA (Shimadzu, EPMA-1720). Powder XRD with Cu K$_\alpha$ radiation (1.5406 Å) was employed to identify the crystalline phases of the cathode materials using Empyrean (PANalytical). The XRD data were collected between 10° and 110° of 2θ with a step size of 0.02°, and analyzed by Rietveld refinement using Fullprof. The in situ XRD experiments on the pouch-type half-cells using Li metal as an anode were performed using transmission mode (Empyrean, PANalytical). The pouch-type half-cells were charged by applying a constant current of 0.05 C (9 mA g^{-1}). The in situ XRD patterns were continuously recorded every 40 min in the 2θ range of 16–70° at a step width of 0.0263° with Cu K$_\alpha$ radiation (1.5406 Å) using a detector (PIXcel 1D, PANalytical). The morphologies and structures

of the prepared active material particles were observed by SEM (Verios G4UC, FEI). The surface area was obtained by N$_2$ adsorption/desorption isotherms using Brunauer–Emmett–Teller (BET, 3 Flex, Micromeritics). For cross-sectional SEM observation, the electrodes were collected in an Ar-filed glovebox at different SOCs and cut by Ar-Ion beam milling using a cooling cross-sectional polisher (CP, JEOL IB-19520CCP) at –90 °C. Then, the electrodes were transferred into an Ar-filed atmosphere from CP to SEM equipment using an Air-Isolation system holder in order to minimize the air-exposure time. For the TEM measurements, active material particles collected from the 100 cycled electrodes at the discharged state were cut into a 70 nm-thick thin foil using a focused ion beam (FIB, SCIOS, FEI) and loaded onto a Mo grid. For ex situ XRD analysis of all-solid-state cells, the collected cells were mounted on the holder and sealed with a Be window in an Ar-filled glove box. The ex situ XRD measurements were conducted using a Rigaku MiniFlex 600 diffractometer with Cu K$_\alpha$ radiation between 10° and 70° of 2θ with a step size of 0.02°. The ex situ XPS measurements were carried out with a monochromatic Al K$_\alpha$ source (1486.6 eV) at 12 kV and 6 mA using K-Alpha+ (Thermo Fisher Scientific). The samples were mounted on a sample holder in an Ar-filled glove box and transferred into the XPS equipment without any exposure to air.

Electrochemical Characterization: For all-solid-state cells, NCM electrodes comprised of cathode materials (NCA80 or FCG75), SE (Li$_6$PS$_5$Cl), and conducting carbon additives (super P) in a weight ratio of 70:30:3 were prepared by dry-mixing using mortar and pestle. Counter electrodes (or anodes) were partially lithiated indium (nominal composition of Li$_{0.5}$In) or Li metal foil (20 µm). The Li$_{0.5}$In was prepared by mixing Li (FMC Lithium corp.) and In (Sigma-Aldrich, 99.99%) powders.[47] All-solid-state cells with a diameter of 13 mm, comprised of Ti rods as the current collectors and polyaryletheretherketone (PEEK) mold, were assembled by the following procedure. First, SE layers were formed by pelletizing 150 mg of Li$_6$PS$_5$Cl powder. Then, the as-prepared cathode mixtures were spread on one side of the SE layer while the counter electrode (Li$_{0.5}$In) was put on the other side. Finally, the whole assemblies were pressed at 370 MPa. The mass loading of the NCM electrodes was 11.3 mg cm^{-2}. For NCM/Li ASLBs tested at 70 °C, the electrode mass loading was 22.6 mg cm^{-2}. EIS measurements were performed for the cells discharged to 3.8 V (vs Li/Li$^+$) at 0.1 C using a Bio-Logic (VMP3) from 1.5 MHz to 10 Hz with an amplitude of 10 mV. The external pressure of the all-solid-state cells during operation were ≈70 and ≈7 MPa when using Li$_{0.5}$In (or Li$_4$Ti$_5$O$_{12}$) and Li metal as the anodes, respectively. For operando electrochemical pressiometry, zero-strain Li$_4$Ti$_5$O$_{12}$ with a negative to positive (np) ratio of 1.3 was used as the anode material. The pressures during charge and discharge were monitored using a pressure sensor, as illustrated in Figure 3j. For the fabrication of the cathode of LE cells, the synthesized cathode active material powders were mixed with carbon black and poly(vinylidene fluoride) (90:5.5:4.5 by weight percents) in *N*-methylpyrrolidone. The obtained slurry was coated on a current collector, Al foil, with active material mass loadings of 4 mg cm^{-2}. The as-prepared electrodes were pressed and dried under vacuum at 120 °C. The LE was 1.2 M LiPF$_6$ in a mixture of ethylene carbonate and ethyl methyl carbonate (volume ratio of 3:7) with 2 wt% vinylene carbonate. Preliminary cell tests were performed using 2032 coin-type half-cells using lithium metal as an anode. The cells were cycled at 0.5 C (100 mA g^{-1}) between 3.0 and 4.3 V.

Supporting Information

Supporting Information is available from the Wiley Online Library or from the author.

Acknowledgements

[1] J. W. Choi, D. Aurbach, *Nat. Rev. Mater.* **2016**, *1*, 16013.
[2] Y. Kato, S. Hori, T. Saito, K. Suzuki, M. Hirayama, A. Mitsui, M. Yonemura, H. Iba, R. Kanno, *Nat. Energy* **2016**, *1*, 16030.
[3] K. H. Park, Q. Bai, D. H. Kim, D. Y. Oh, Y. Zhu, Y. Mo, Y. S. Jung, *Adv. Energy Mater.* **2018**, *8*, 1800035.
[4] J. Kalhoff, G. G. Eshetu, D. Bresser, S. Passerini, *ChemSusChem* **2015**, *8*, 2154.
[5] K. Liu, Y. Liu, D. Lin, A. Pei, Y. Cui, *Sci. Adv.* **2018**, *4*, eaas9820.
[6] X.-B. Cheng, R. Zhang, C.-Z. Zhao, Q. Zhang, *Chem. Rev.* **2017**, *117*, 10403.
[7] P. Albertus, S. Babinec, S. Litzelman, A. Newman, *Nat. Energy* **2018**, *3*, 16.
[8] J. C. Bachman, S. Muy, A. Grimaud, H.-H. Chang, N. Pour, S. F. Lux, O. Paschos, F. Maglia, S. Lupart, P. Lamp, L. Giordano, Y. Shao-Horn, *Chem. Rev.* **2016**, *116*, 140.
[9] J. Janek, W. G. Zeier, *Nat. Energy* **2016**, *1*, 16141.
[10] A. Manthiram, X. Yu, S. Wang, *Nat. Rev. Mater.* **2017**, *2*, 16103.
[11] Z. Zhang, Y. Shao, B. Lotsch, Y.-S. Hu, H. Li, J. Janek, L. F. Nazar, C.-W. Nan, J. Maier, M. Armand, L. Chen, *Energy Environ. Sci.* **2018**, *11*, 1945.
[12] Z. Liu, W. Fu, E. A. Payzant, X. Yu, Z. Wu, N. J. Dudney, J. Kiggans, K. Hong, A. J. Rondinone, C. Liang, *J. Am. Chem. Soc.* **2013**, *135*, 975.
[13] L. Duchêne, R. S. Kühnel, D. Rentsch, A. Remhof, H. Hagemann, C. Battaglia, *Chem. Commun.* **2017**, *53*, 4195.
[14] F. Han, A. S. Westover, J. Yue, X. Fan, F. Wang, M. Chi, D. N. Leonard, N. J. Dudney, H. Wang, C. Wang, *Nat. Energy* **2019**, *4*, 187.
[15] X. Yao, D. Liu, C. Wang, P. Long, G. Peng, Y.-S. Hu, H. Li, L. Chen, X. Xu, *Nano Lett.* **2016**, *16*, 7148.
[16] N. Kamaya, K. Homma, Y. Yamakawa, M. Hirayama, R. Kanno, M. Yonemura, T. Kamiyama, Y. Kato, S. Hama, K. Kawamoto, A. Mitsui, *Nat. Mater.* **2011**, *10*, 682.
[17] Y. Seino, T. Ota, K. Takada, A. Hayashi, M. Tatsumisago, *Energy Environ. Sci.* **2014**, *7*, 627.
[18] H.-J. Deiseroth, S.-T. Kong, H. Eckert, J. Vannahme, C. Reiner, T. Zaiss, M. Schlosser, *Angew. Chem., Int. Ed.* **2008**, *47*, 755.
[19] P. Adeli, J. D. Bazak, K. H. Park, I. Kochetkov, A. Huq, G. R. Goward, L. F. Nazar, *Angew. Chem., Int. Ed.* **2019**, *58*, 8681.
[20] K. H. Park, D. Y. Oh, Y. E. Choi, Y. J. Nam, L. Han, J.-Y. Kim, H. Xin, F. Lin, S. M. Oh, Y. S. Jung, *Adv. Mater.* **2016**, *28*, 1874.
[21] Y. Liu, Q. Sun, D. Wang, K. Adair, J. Liang, X. Sun, *J. Power Sources* **2018**, *393*, 193.

[22] S. Ito, S. Fujiki, T. Yamada, Y. Aihara, Y. Park, T. Y. Kim, S.-W. Baek, J.-M. Lee, S. Doo, N. Machida, *J. Power Sources* **2014**, *248*, 943.
[23] Y. J. Nam, D. Y. Oh, S. H. Jung, Y. S. Jung, *J. Power Sources* **2018**, *375*, 93.
[24] S. H. Jung, K. Oh, Y. J. Nam, D. Y. Oh, P. Bruener, K. Kang, Y. S. Jung, *Chem. Mater.* **2018**, *30*, 8190.
[25] D. Y. Oh, Y. J. Nam, K. H. Park, S. H. Jung, K. T. Kim, A. R. Ha, Y. S. Jung, *Adv. Energy Mater.* **2019**, *9*, 1802927.
[26] D. H. Kim, D. Y. Oh, K. H. Park, Y. E. Choi, Y. J. Nam, H. A. Lee, S.-M. Lee, Y. S. Jung, *Nano Lett.* **2017**, *17*, 3013.
[27] A. Sakuda, A. Hayashi, M. Tatsumisago, *Chem. Mater.* **2010**, *22*, 949.
[28] K. Takada, *Langmuir* **2013**, *29*, 7538.
[29] Y. Zhu, X. He, Y. Mo, *J. Mater. Chem. A* **2016**, *4*, 3253.
[30] Z. Wang, D. Santhanagopalan, W. Zhang, F. Wang, H. L. Xin, K. He, J. Li, N. Dudney, Y. S. Meng, *Nano Lett.* **2016**, *16*, 3760.
[31] J. Auvergniot, A. Cassel, J. B. Ledeuil, V. Viallet, V. Seznec, R. Dedryvere, *Chem. Mater.* **2017**, *29*, 3883.
[32] Y. Xiao, L. J. Miara, Y. Wang, G. Ceder, *Joule* **2019**, *3*, 1252.
[33] F. Walther, R. Koerver, T. Fuchs, S. Ohno, J. Sann, M. Rohnke, W. G. Zeier, J. Janek, *Chem. Mater.* **2019**, *31*, 3745.
[34] B. R. Shin, Y. J. Nam, D. Y. Oh, D. H. Kim, J. W. Kim, Y. S. Jung, *Electrochim. Acta* **2014**, *146*, 395.
[35] Y. Zhu, X. He, Y. Mo, *ACS Appl. Mater. Interfaces* **2015**, *7*, 23685.
[36] S. Wenzel, T. Leichtweiss, D. A. Weber, J. Sann, W. G. Zeier, J. Janek, *ACS Appl. Mater. Interfaces* **2016**, *8*, 28216.
[37] N. Ohta, K. Takada, L. Zhang, R. Ma, M. Osada, T. Sasaki, *Adv. Mater.* **2006**, *18*, 2226.
[38] N. Ohta, K. Takada, I. Sakaguchi, L. Zhang, R. Ma, K. Fukuda, M. Osada, T. Sasaki, *Electrochem. Commun.* **2007**, *9*, 1486.
[39] J. H. Woo, J. J. Travis, S. M. George, S.-H. Lee, *J. Electrochem. Soc.* **2015**, *162*, A344.
[40] Y. S. Jung, A. S. Cavanagh, L. A. Riley, S. H. Kang, A. C. Dillon, M. D. Groner, S. M. George, S. H. Lee, *Adv. Mater.* **2010**, *22*, 2172.
[41] J. R. Dahn, U. von Sacken, C. A. Michal, *Solid State Ionics* **1990**, *44*, 87.
[42] H. J. Noh, S. Youn, C. S. Yoon, Y.-K. Sun, *J. Power Sources* **2013**, *233*, 121.
[43] K.-J. Park, J.-Y. Hwang, H.-H. Ryu, F. Maglia, S.-J. Kim, P. Lamp, C. S. Yoon, Y.-K. Sun, *ACS Energy Lett.* **2019**, *4*, 1394.
[44] W. Lee, S. Muhammad, C. Sergey, H. Lee, J. Yoon, Y. M. Kang, W.-S. Yoon, *Angew. Chem., Int. Ed.* **2019**, *58*, 2.
[45] D. Y. Oh, D. H. Kim, S. H. Jung, J.-G. Han, N.-S. Choi, Y. S. Jung, *J. Mater. Chem. A* **2017**, *5*, 20771.
[46] R. Koerver, I. Aygün, T. Leichtweiß, C. Dietrich, W. Zhang, J. O. Binder, P. Hartmann, W. G. Zeier, J. Janek, *Chem. Mater.* **2017**, *29*, 5574.
[47] Y. J. Nam, K. H. Park, D. Y. Oh, W. H. An, Y. S. Jung, *J. Mater. Chem. A* **2018**, *6*, 14867.
[48] R. Koerver, W. Zhang, L. d. Biasi, S. Schweidler, A. O. Kondrakov, S. Kolling, T. Brezesinski, P. Hartmann, W. G. Zeier, J. Janek, *Energy Environ. Sci.* **2018**, *11*, 2142.
[49] J.-H. Kim, H.-H. Ryu, S. J. Kim, C. S. Yoon, Y.-K. Sun, *ACS Appl. Mater. Interfaces* **2019**, *11*, 30936.
[50] R. Schmuch, R. Wagner, G. Hörpel, T. Placke, M. Winter, *Nat. Energy* **2018**, *3*, 267.
[51] H.-H. Ryu, K.-J. Park, C. S. Yoon, Y.-K. Sun, *Chem. Mater.* **2018**, *30*, 1155.
[52] U.-H. Kim, H.-H. Ryu, J.-H. Kim, R. Mücke, P. Kaghazchi, C. S. Yoon, Y.-K. Sun, *Adv. Energy Mater.* **2019**, *9*, 1803902.
[53] Y. Yang, R. Xu, K. Zhang, S.-J. Lee, L. Mu, P. Liu, C. K. Waters, S. Spence, Z. Xu, C. Wei, D. J. Kautz, Q. Yuan, Y. Dong, Y.-S. Yu, X. Xiao, H.-K. Lee, P. Pianetta, P. Cloetens, J.-S. Lee, K. Zhao, F. Lin, Y. Liu, *Adv. Energy Mater.* **2019**, *9*, 1900674.

ADVANCED
SCIENCE NEWS

www.advancedsciencenews.com

ADVANCED
ENERGY
MATERIALS

www.advenergymat.de

[54] Y.-K. Sun, S.-T. Myung, B.-C. Park, J. Prakash, I. Belharouak, K. Amine, *Nat. Mater.* **2009**, *8*, 320.

[55] Y.-K. Sun, Z. Chen, H.-J. Noh, D.-J. Lee, H.-G. Jung, Y. Ren, S. Wang, C. S. Yoon, S.-T. Myung, K. Amine, *Nat. Mater.* **2012**, *11*, 942.

[56] C. S. Yoon, K. J. Park, U. H. Kim, K. H. Kang, H. H. Ryu, Y.-K. Sun, *Chem. Mater.* **2017**, *29*, 10436.

[57] A. Zaban, E. Zinigrad, D. Aurbach, *J. Phys. Chem.* **1996**, *100*, 3089.

[58] Y. J. Nam, S. J. Jo, D. Y. Oh, J. M. Im, S. Y. Kim, J. H. Song, Y. G. Lee, S.-Y. Lee, Y. S. Jung, *Nano Lett.* **2015**, *15*, 3317.

[59] W. Li, J. N. Reimers, J. R. Dahn, *Solid State Ionics* **1993**, *67*, 123.

[60] C. S. Yoon, D. W. Jun, S. T. Myung, Y.-K. Sun, *ACS Energy Lett.* **2017**, *2*, 1150.

[61] W. Zhang, D. A. Weber, H. Weigand, T. Arlt, I. Manke, D. Schröder, R. Koerver, T. Leichtweiss, P. Hartmann, W. G. Zeier, J. Janek, *ACS Appl. Mater. Interfaces* **2017**, *9*, 17835.

[62] X. Wu, J. Billaud, I. Jerjen, F. Marone, Y. Ishihara, M. Adachi, Y. Adachi, C. Villevieille, Y. Kato, *Adv. Energy Mater.* **2019**, *9*, 1901547.

[63] J. H. Kim, S. J. Kim, T. Yuk, J. Kim, C. S. Yoon, Y.-K. Sun, *ACS Energy Lett.* **2018**, *3*, 3002.

[64] F. P. McGrogan, T. Swamy, S. R. Bishop, E. Eggleton, L. Porz, X. Chen, Y.-M. Chiang, K. J. V. Vliet, *Adv. Energy Mater.* **2017**, *7*, 1602011.

[65] H. Arai, M. Tsuda, K. Saito, M. Hayashi, K. Takei, Y. Sakurai, *J. Solid State Chem.* **2002**, *163*, 340.

[66] S. Watanabe, M. Kinoshita, T. Hosokawa, K. Morigaki, K. Nakura, *J. Power Sources* **2014**, *258*, 210.

[67] J. Auvergniot, A. Cassel, D. Foix, V. Viallet, V. Seznec, R. Dedryvere, *Solid State Ionics* **2017**, *300*, 78.

[68] T. Asano, A. Sakai, S. Ouchi, M. Sakaida, A. Miyazaki, S. Hasegawa, *Adv. Mater.* **2018**, *30*, 1803075.

[69] Energy Storage System Goals, USCAR (United States Council for Automotive Research LLC), https://www.uscar.org/guest/article_view.php?articles_id=85 (accessed: July 2019).

1903360 (12 of 12)